AGU PUBLICATIONS

Geophysical Research Letters

RESEARCH LETTER
10.1002/2017GL076124

Key Points:
- We compute the cumulative seismic moment due to convective and cooling stresses from 3-D thermal evolution models of Mars
- The annual seismic moment budget calculated from our models is between 5.7×10^{16} and 3.9×10^{19} Nm
- A new, self-consistent model for the spatial distribution of seismicity is derived from 3-D thermal evolution models

Supporting Information:
- Supporting Information S1
- Data Set S1
- Data Set S2
- Data Set S3
- Data Set S4
- Data Set S5
- Data Set S6
- Data Set S7
- Data Set S8
- Data Set S9
- Data Set S10
- Data Set S11
- Data Set S12

Correspondence to:
A.-C. Plesa,
ana.plesa@dlr.de

Citation:
Plesa, A.-C., Knapmeyer, M., Golombek, M. P., Breuer, D., Grott, M., Kawamura, T., et al. (2018). Present-day Mars' seismicity predicted from 3-D thermal evolution models of interior dynamics. *Geophysical Research Letters*, *45*, 2580–2589. https://doi.org/10.1002/2017GL076124

Received 20 OCT 2017
Accepted 19 FEB 2018
Accepted article online 27 FEB 2018
Published online 30 MAR 2018

Present-Day Mars' Seismicity Predicted From 3-D Thermal Evolution Models of Interior Dynamics

A.-C. Plesa[1], M. Knapmeyer[1], M. P. Golombek[2], D. Breuer[1], M. Grott[1], T. Kawamura[3,4], P. Lognonné[3], N. Tosi[1,5], and R. C. Weber[6]

[1]German Aerospace Center (DLR), Berlin, Germany, [2]Jet Propulsion Laboratory, California Institute of Technology, Pasadena, CA, USA, [3]Institut de Physique du Globe de Paris, Université Paris Diderot – Sorbonne Paris Cité, Paris, France, [4]National Astronomical Observatory of Japan, Oshu, Japan, [5]Technische Universität Berlin, Berlin, Germany, [6]NASA Marshall Space Flight Center, Huntsville, AL, USA

Abstract The Interior Exploration using Seismic Investigations, Geodesy and Heat Transport mission, to be launched in 2018, will perform a comprehensive geophysical investigation of Mars in situ. The Seismic Experiment for Interior Structure package aims to detect global and regional seismic events and in turn offer constraints on core size, crustal thickness, and core, mantle, and crustal composition. In this study, we estimate the present-day amount and distribution of seismicity using 3-D numerical thermal evolution models of Mars, taking into account contributions from convective stresses as well as from stresses associated with cooling and planetary contraction. Defining the seismogenic lithosphere by an isotherm and assuming two end-member cases of 573 K and the 1073 K, we determine the seismogenic lithosphere thickness. Assuming a seismic efficiency between 0.025 and 1, this thickness is used to estimate the total annual seismic moment budget, and our models show values between 5.7×10^{16} and 3.9×10^{19} Nm.

1. Introduction

The level of seismicity on Mars is usually believed to lie between that of the Earth and the Moon. Based on the seismic events recorded between 1976 and 2013 and documented in the Harvard Centroid Moment Tensor catalog, the annual seismic moment release for the Earth is $\sim 3 \times 10^{23}$ Nm. The values for the Moon are significantly lower and range between 10^{14} and 10^{15} Nm only for the shallow moonquakes (Oberst, 1987) and below 10^{14} Nm for deep moonquakes (Kawamura et al., 2017). For Mars, only indirect estimates exist, which are based on the analysis of surface faults and models of lithospheric cooling (e.g., Golombek et al., 1992; Knapmeyer et al., 2006; Phillips, 1991). The upcoming Discovery class mission InSight (Interior Exploration using Seismic Investigations, Geodesy and Heat Transport) to be launched in 2018 will employ a seismometer (Seismic Experiment for Interior Structure) (Lognonné et al., 2015), a heat flow probe (Heat Flow and Physical Properties Package) (Spohn et al., 2014), and precision tracking system (Dehant et al., 2011) to accurately measure the present-day seismic activity and the rate at which heat is lost from the planet (Banerdt et al., 2012, 2017). Such measurements will provide an important baseline to constrain the present-day interior structure and heat budget of the planet and, in turn, the thermal and chemical evolution of its interior.

Previous seismic measurements on Mars were performed in the mid-1970s by the Viking seismic experiment (Anderson et al., 1976). The Viking 1 seismometer failed to uncage, and no data were recorded. However, the Viking 2 lander performed seismic measurements with a short-period three-component seismometer in Utopia Planitia and collected data between September 1976 and April 1978. The installation of the seismometer on top of the lander instrument deck led to a high noise level produced by wind-induced movements of the lander. During the 146 sols of operation of the Viking 2 seismometer, only one event during sol 80 was recorded, which might be interpreted as a local marsquake. However, the absence of wind data during the sol 80 signal makes it difficult to unambiguously catalog it as being of seismic origin. Nevertheless, a recent study suggests that a wind gust can be excluded as a source because of the low wind speeds recorded 20 min before and 45 min after this event (Lorenz et al., 2017).

The nondetection of unambiguous marsquakes led to the conclusion that Mars' seismicity is smaller than that of the Earth (Anderson et al., 1977). Indeed, the analysis of surface faults suggests moment releases between 10^{17} and 10^{19} Nm/year (Golombek, 2002; Golombek et al., 1992), while studies taking into account global

cooling of the planet suggest values between 3.42×10^{16} and 4.78×10^{18} Nm/year (Knapmeyer et al., 2006; Phillips, 1991). Along with assumptions about the largest marsquake and the moment-frequency relation, the total moment release can be ascribed to the frequency of individual marsquakes of different moment release. However, the spatial distribution of present-day seismicity on Mars is only indirectly constrained and previous work has focused on mapping the distribution of visible surface tectonic faults, as these features may hint at the internal stress field distribution (e.g., Banerdt et al., 1992; Carr, 1974; Golombek & Phillips, 2009; Wise et al., 1979). Previous mapping campaigns have focused on not only local features (Anderson et al., 2004; Hauber & Kronberg, 2001, 2005; Tanaka, 1990; Tanaka & Davis, 1988) but also prominent fault systems associated with Tharsis (e.g., Anderson et al., 2004; Banerdt et al., 1992; Tanaka et al., 1991). Using Viking Orbiter imagery, Anderson et al. (2001) mapped the surface faults on the entire western hemisphere, while Anderson et al. (2008) compiled a paleotectonic map of the eastern hemisphere to identify centers of tectonic activity. A study by Knapmeyer et al. (2006) derived a global fault catalog using Mars Orbiting Laser Altimeter shaded topographic relief maps. Using this global catalog, Knapmeyer et al. (2006) suggested a distribution of epicenters by associating individual event sizes with individual fault length, such that small events may occur on almost any fault, while large events occur only on faults large enough to produce them. However, it remains uncertain which of the faults are currently active on Mars.

Of particular interest for InSight are the estimates of seismicity on Cerberus Fossae (Taylor et al., 2013), one of the youngest tectonic features on Mars that is only ~1,500 km to the east-northeast from the InSight landing site. Estimates of moment release indicate recent marsquakes large enough to be recorded by the InSight instruments (Taylor et al., 2013).

In this study, we use models of the thermal evolution of Mars in a 3-D spherical geometry to assess the amount and distribution of present-day seismicity. While previous studies have used stresses associated with cooling and planetary contraction to estimate the amount of seismicity of Mars, convective stresses have not been considered so far but can represent an important contribution to the annual seismic moment budget. In addition, 3-D thermal evolution models can be used to self-consistently derive the spatial distribution of present-day seismicity on Mars. As the InSight lander will perform its measurements at a single designated location in the Elysium Planitia region (Golombek et al., 2017), numerical simulations of planetary interiors can be used to interpret the data in a global context.

2. Model

2.1. Thermal Evolution Model

We employ the thermal evolution models in 3-D spherical geometry presented in Plesa et al. (2016). By extending the parameter space, we perform additional simulations to collect a number of cases for which we can carry out statistical analysis. In addition to solving the conservation equations of mass, linear momentum, and thermal energy, our models account for core cooling and the decay of heat-producing elements (HPE). We consider adiabatic heating and cooling by using the extended Boussinesq approximation (King et al., 2010). Our models use a crust whose thickness does not change with time but varies laterally as inferred from gravity and topography data (Neumann et al., 2004; Plesa et al., 2016). We use the compositional model of Wänke and Dreibus (1994) and partition the HPE between the mantle and crust such that the present-day surface abundances match the average value inferred from gamma ray measurements (Hahn et al., 2011; Taylor et al., 2006). Because the crustal thickness shows larger variations than the surface abundance of HPE, we neglect spatial variations in crustal HPE and use an average concentration of 49 pW/kg at present day (Hahn et al., 2011). In addition, we consider the blanketing effect of the crust by using a lower thermal conductivity in the crust compared to the mantle. This leads to higher temperatures in mantle regions covered by a thick crust compared to regions covered by a thin crust. A detailed model description is shown in section S1 of the supporting information (SI) and in Plesa et al. (2016). Input parameters for each individual simulation are listed in Table S3 of the SI.

Plesa et al. (2016) have shown that the structure and thickness of the crust play an important role in the distribution and magnitude of the surface heat flow and the elastic lithosphere thickness. For the present study, we have selected three end-member crustal thickness models, which are consistent with current gravity and topography data. We note that a recently published crustal thickness model by Goossens et al. (2017), which includes a spatially variable crustal density with an average value of only $2{,}582 \pm 209$ kg/m^3, leads to a different crustal thickness pattern. This kind of model will be addressed in future studies. The "density dichotomy

crust" (DC) model, which uses a crustal density of 2,900 kg/m^3 for the southern highlands and 3,100 kg/m^3 for the northern lowlands, shows a relatively uniform crustal thickness distribution apart from the Tharsis region (Plesa et al., 2016). The "high density crust" (HC) model, which uses a uniform crustal density of 3,200 kg/m^3, exhibits the most pronounced variations in crustal thickness (Plesa et al., 2016). The model by Neumann et al. (2004) (NC model), which assumes a lower uniform crustal density of 2,900 kg/m^3, is intermediate between the previous two (Figure S1 of the SI).

2.2. Seismicity Model

We use our thermal evolution models to compute the present-day annual cumulative seismic moment budget M_{cum} following Knapmeyer et al. (2006):

$$M_{\text{cum}} = \eta \dot{\varepsilon} V \mu \Delta t \tag{1}$$

where η is the seismic efficiency, a scale factor that determines how much of the actual deformation is released in the form of seismic energy (discussed below). $\dot{\varepsilon}$ is the strain rate computed from the thermal evolution model, and V is the seismogenic volume, which we calculated based on the depth of the 573 K or 1073 K mantle isotherms. The 573 K isotherm is often associated with the bottom of the seismogenic layer since this is the temperature above which quartz, the most ductile component of a granitic crust, shows a plastic behavior (Scholz, 1998). Although the presence of quartzo-feldspathic material has been identified in the lower units of Valles Marineris and in localized regions in the southern highlands (Bandfield et al., 2004), and granodiorite-like rocks have been analyzed in Gale crater (Sautter et al., 2016), the majority of the Martian crust is considered to be basaltic to andesitic in composition (e.g., Zuber, 2001). For this type of materials, the 1073 K isotherm marks the maximum depth of oceanic intraplate quakes on the Earth (Bergman, 1986; Wiens & Stein, 1983) and we will assume this to be the upper limit for the seismogenic layer thickness on Mars. We varied the shear modulus μ between 30 and 70 GPa. The time interval Δt is set here to 1 year to obtain the annual seismic moment budget in the sense of the moment conservation principle. We compute the cumulative seismic moment on a $3^\circ \times 3^\circ$ grid to filter out small-scale structures that may be specific for an individual simulation, given that we are interested in features associated with large geologic regions such as the Tharsis and Elysium volcanic provinces, and large impact basins (e.g., Hellas).

The seismic efficiency factor η describes how much strain is released in seismic events compared to aseismic deformation (i.e., folding and aseismic creep). For the Earth, Ward (1998a) and Ward (1998b) derived the seismic efficiency from the ratio of seismic to geodetic moment rates and found large regional variations between 0.025 and 0.86, depending on location. While values above 0.7 are representative for Southern and Northern California regions located close to the boundary between North American and Pacific plates, smaller values of only a few percent are representative for slow-straining regions, for example, central USA and northwest Europe. The small values, however, are attributed to lack of long-term observational data (Ward, 1998a). In this study, we varied the seismic efficiency between 0.025 and 1.

In equation (1) the strain rate is computed either taking into account the convective stresses or stresses produced by planetary contraction. If the former are used, $\dot{\varepsilon}$ is calculated as the second invariant of the strain rate tensor:

$$\dot{\varepsilon} = \left(\sum_{ij} \dot{\varepsilon}_{ij} \dot{\varepsilon}_{ij} \right)^{1/2} \tag{2}$$

where $\dot{\varepsilon}_{ij} = \frac{1}{2}\left(\frac{\partial v_i}{\partial x_j} + \frac{\partial v_j}{\partial x_i} \right)$ and $\frac{\partial v_i}{\partial x_j}$ is the spatial gradient of the velocity vector. We calculate equation (2) throughout the seismogenic layer. In a stagnant lid planet convective stresses become smaller the shallower the depth is. However, if the seismogenic layer is defined by the 1073 K isotherm, it will reach depths where strain rate values become nonnegligible (for a typical strain rate profile, see Figure S4 of the SI).

When considering stresses produced by mantle cooling and planetary contraction, $\dot{\varepsilon}$ is related to the planetary radius change due to core and mantle heating or cooling:

$$\dot{\varepsilon} = \frac{\Delta R}{R_{l/2}} \frac{1}{\Delta t} \tag{3}$$

where $R_{1/2}$ is the radius corresponding to half the present-day seismogenic layer volume and Δt is the time interval over which the radius change (ΔR) is computed. The radius change is calculated column wise using

the temperature profile beneath each surface grid point. We employ the same approach as Grott et al. (2011) and Tosi et al. (2013) but use the radius $R_{l/2}$ instead of the planetary radius:

$$\Delta R = \alpha_c(T_c(t_n) - T_c(t_{n-1}))\frac{R_c^3}{3R_{l/2}^2} + \frac{1}{R_{l/2}^2}\int_{R_c}^{R_{l/2}} \alpha_m(T_m(r,t_n) - T_m(r,t_{n-1}))r^2 \mathrm{d}r \quad (4)$$

where α_c and α_m are the thermal expansion coefficients of the core and mantle, T_c and $T_m(r)$ are the core-mantle boundary (CMB) temperature and the mantle temperature, and R_c is the radius of the core. We choose $R_{l/2}$ instead of the planetary radius R_p or the radius at the base of the seismogenic layer, R_l, because we compute an average radius change in the seismogenic layer. The radius change obtained when using R_p overestimates the actual ΔR that takes place in the seismogenic layer, while the radius change calculated using R_l underestimates it. In contrast to the previous studies of Phillips (1991) and Knapmeyer et al. (2006) who only computed the radius change within the seismogenic layer, we take into account the contraction of the core and the entire mantle up to the radius $R_{l/2}$. Our models use a time output resolution of 10 Myr, and since we are interested in the present-day seismic moment, we compute the radius change based on the temperatures at 4.49 Gyr and at present day. Hence, $T_c(t_n)$ and $T_m(r, t_n)$ refer to the present day CMB and mantle temperature, respectively, while $T_c(t_{n-1})$ and $T_m(r, t_{n-1})$ are the CMB and mantle temperature after 4.49 Gyr of evolution, respectively. Accordingly, Δt in equation (3) is set to 10 Myr.

3. Results

We compute the seismic moment budget for each thermal evolution simulation using the parameters listed in Table S1 of the SI, and for each crustal thickness model we calculate the median of at least eight simulations in every 3° × 3° grid region.

Our models show an annual seismic moment budget between 5.7×10^{16} Nm and 3.9×10^{19} Nm. The minimum value is obtained by assuming the 573 K isotherm to define the seismogenic layer volume, a seismic efficiency of 0.025, and a shear modulus of 30 GPa and using the median of simulations employing the NC model, which shows the lowest seismic moment budget. The maximum value is computed by assuming the 1073 K isotherm to define the seismogenic layer volume, a seismic efficiency of 1, and a shear modulus of 70 GPa and using the median of simulations employing the HC model, which shows the highest seismic moment budget. In our models, the annual seismic moment budget can reach values higher than 1.95×10^{19} Nm only if the seismic efficiency is larger than 0.5 and rather close to 1, while values below 10^{17} Nm necessarily require $\eta < 0.05$ (Table S2 of the SI).

Figure 1 shows histograms of the seismogenic depth for all models studied here using either the 573 K (Figure 1a) or 1073 K (Figure 1b) isotherm to compute the seismogenic volume. The simulations employing the NC and DC model show a similar distribution with a pronounced peak at around 50 km for the 573 K isotherm and around 170 km for the 1073 K isotherm. The HC model exhibits the highest peak-to-peak crustal thickness variations. This is also reflected in the highest peak-to-peak seismogenic depth variations. In fact, the crustal thickness and the crustal enrichment in HPE influence the temperature distribution in the shallow mantle and consequently regions of thick crust overlie a hotter mantle compared to regions covered by a thinner crust. This effect is most significant for the HC model with a mean crustal thickness of 87 km compared to the other two crustal thickness models, for which the average crustal thickness lies around 45 km. Because the seismogenic depth has been computed based on an isotherm value of 573 and 1073 K, the histograms show the depths at which these values have been attained. While for the NC and the DC model the seismogenic depth lies between 30 and 100 km for the 573 K isotherm, and between 50 km and 250 km for the 1073 K isotherm, the HC model exhibits a much wider range due to the larger variations in crustal thickness and the overall thicker crust. For this end-member crustal thickness model, the seismogenic depth varies between 30 and 170 km for the 573 K isotherm, and between 60 and 450 km for the 1073 K isotherm. In particular, the 1073 K isotherm suggests that, for the HC model, marsquakes could originate at greater depths than assumed in previous studies.

In Figure 2 we illustrate the seismic moment contributions calculated from stresses associated with planetary cooling (Figure 2a) and convective stresses (Figure 2b) as well as the sum of the two (Figure 2c) using the 1073 K isotherm and the HC model of Plesa et al. (2016) as an example (other crustal thickness models are shown in the SI). If we consider stresses associated with cooling and planetary contraction, due to the less

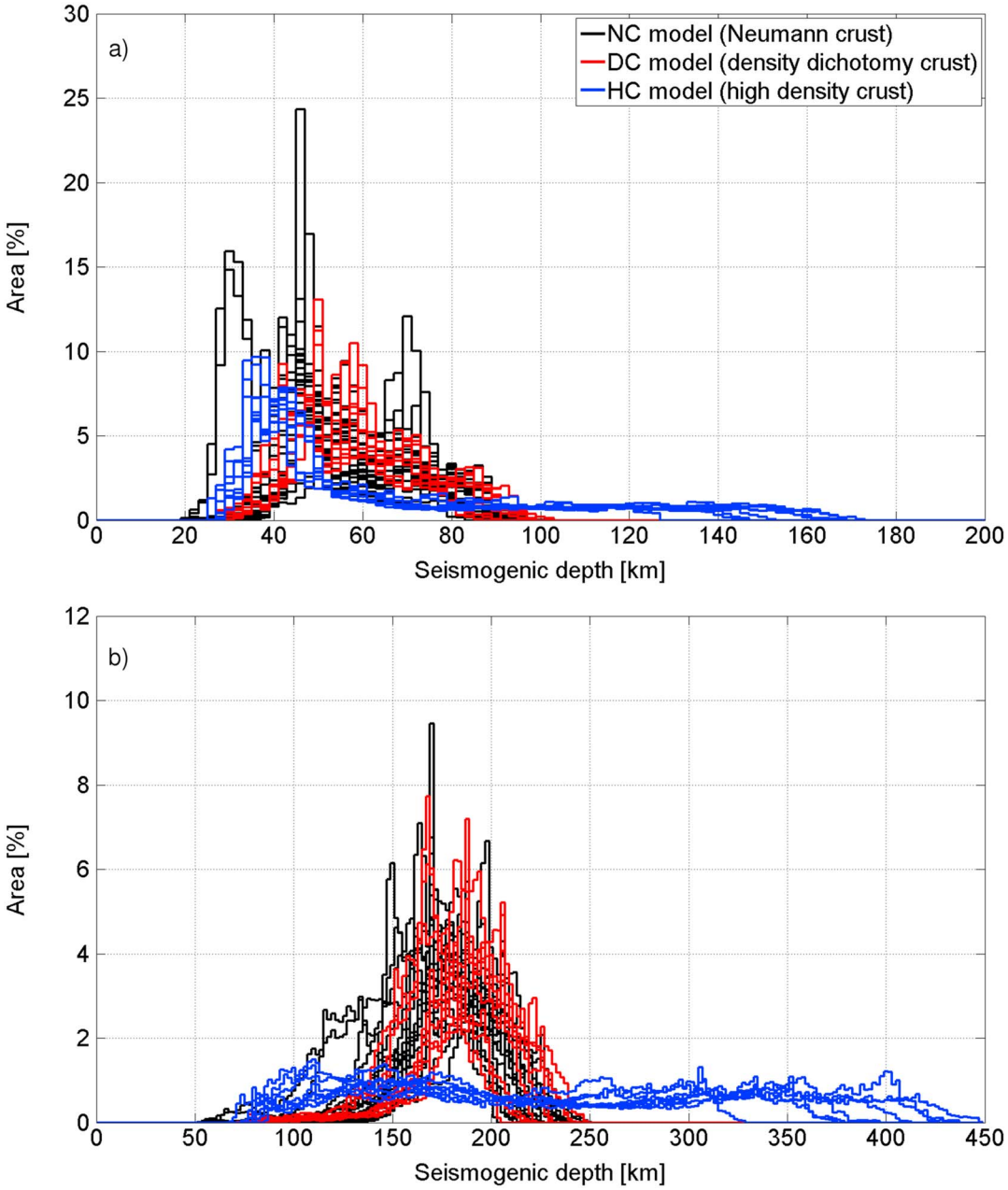

Figure 1. Seismogenic lithosphere thickness: Each line corresponds to a thermal evolution model. (a) The results obtained using the 573 K isotherm. (b) The 1073 K isotherm. Results using the DC model are shown by red lines, simulations using the NC model are shown by black lines, while the DC model is shown by blue lines. The DC and NC models indicate a similar range of seismogenic lithosphere thicknesses, while the HC model shows a much wider range (blue lines). NC = Neumann crustal thickness model; DC = density dichotomy crust; HC = high density crust.

efficient insulation of the crust, the highest values for seismic moment budget are attained in regions of thin crust (i.e., impact basins) and the northern hemisphere. In contrast, regions covered by a thick crust show an inefficient cooling and thus the lowest values of seismic moment budget. If, instead, the seismic moment budget is computed by taking into account convective stresses, the highest seismic moment values are associated with regions where a thick crust is blanketing the underlying mantle. In such regions, higher temperature in the mantle leads to more pronounced deformation and thus higher convective stresses. Hence, the two seismic moment contributions are spatially anticorrelated and their sum (Figure 2c) shows a relatively homogeneous distribution with relative highs in seismic moment from convective stresses.

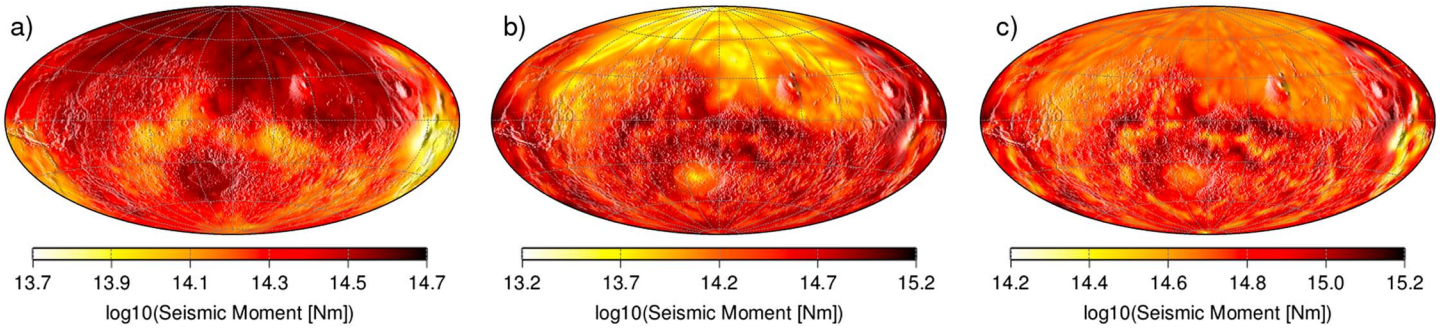

Figure 2. Spatial distribution of the annual seismic moment budget based on (a) the stresses produced by mantle cooling, (b) convective stresses, and (c) the sum of the two contributions. Here we use the HC model of Plesa et al. (2016) and define the seismogenic volume using the depth of the 1073 K isotherm. The seismic efficiency is set here to 1 and the shear modulus to 70 GPa.

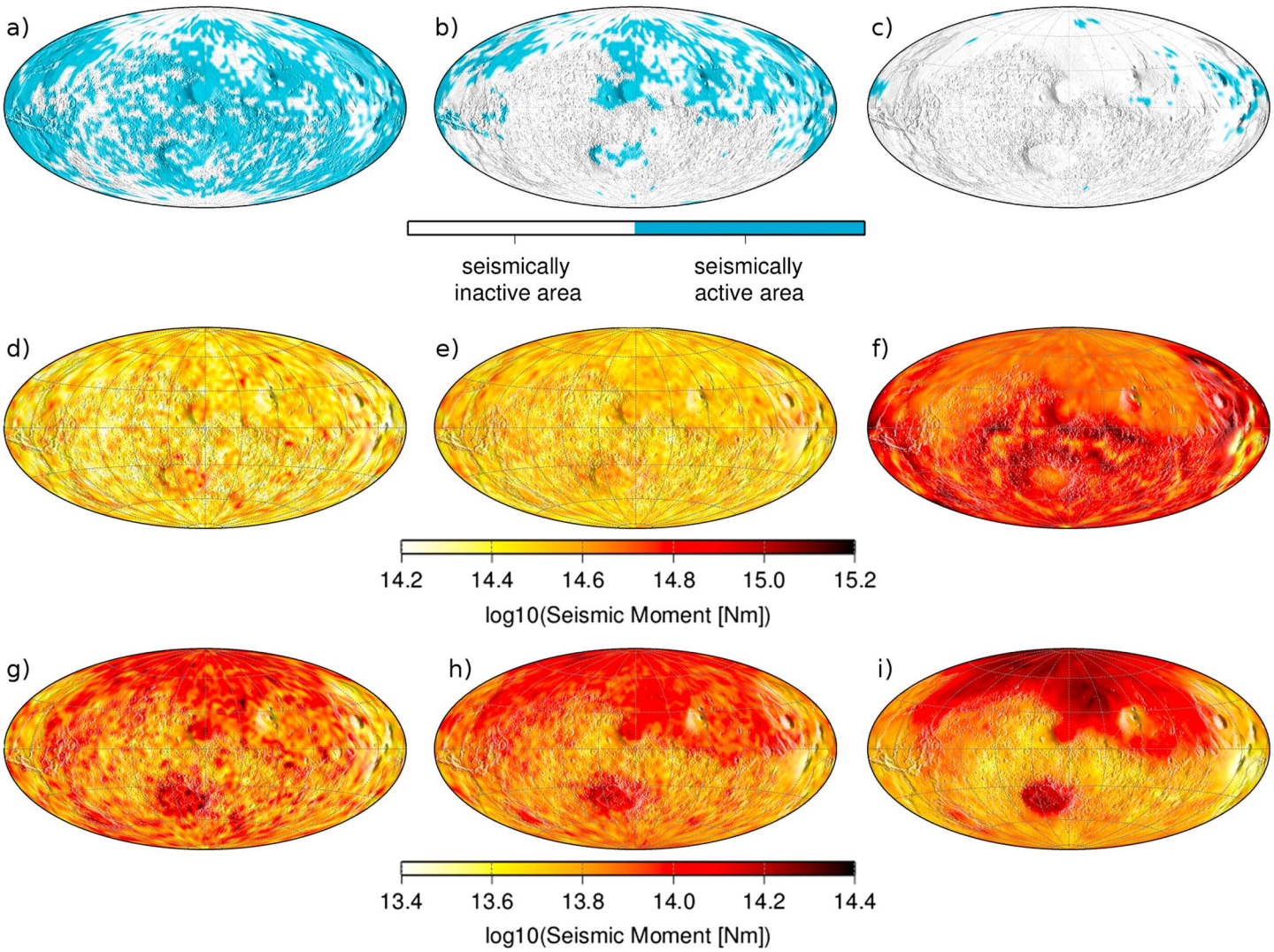

Figure 3. Geographic distribution of possibly seismically active areas based on the fault catalog of Knapmeyer et al. (2006). (a) all faults considered, (b) only faults cutting areas with ages younger than the Noachian epoch (age < 3700 Myr), and (c) only faults on surfaces dated to early Amazonian epoch (age < 600 Myr). White regions on the maps represent areas with zero seismic moment. Spatial distribution of the annual seismic moment budget based on 3-D thermal evolution models that consider both stresses associated with planetary contraction and convective stresses. The total annual seismic moment budget has been calculated using the (d–f) 1073 K isotherm and (g–i) 573 K isotherm. Results based on the DC model are shown in Figures 3d and 3g, on the NC model in Figures 3e and 3h, and on the HC model in Figures 3f and 3i.

We compare our geographic seismic moment distribution with the seismicity distribution on the individual faults mapped by Knapmeyer et al. (2006), discretized on a 3° × 3° grid. Figures 3a–3c show the geographic distribution assuming that certain faults contained in the fault catalog of Knapmeyer et al. (2006) are seismically active. For all three cases, the presence or absence of faults creates an on-off pattern with aseismic areas. The younger the age of the surfaces considered to be seismically active, the smaller the areas where a nonzero seismic moment is attained. The distribution ranges from a nearly homogeneous map, if all faults are considered seismically active (Figure 3a), to limited regions in Tharsis, Elysium, and the northern latitudes if only faults cutting Amazonian surfaces are used (Figure 3c). Figures 3a–3c show that the distribution of surface faults cannot constrain the spatial distribution of seismicity on Mars since it is not known which faults are still active today.

In comparison, the seismic moment distribution predicted by the 3-D thermal evolution models used in this study shows a more homogeneous pattern with all regions being seismically active (Figures 3d–3i). In particular, for the 1073 K isotherm the seismic moment shows a homogeneous distribution for the DC and NC models (Figures 3d and 3e). For the HC models, slightly larger seismic moment values are obtained in regions covered by a thick crust (Figure 3f). While convective stresses are similar in magnitude but spatially anticorrelated with the stresses associated with planetary cooling for the 1073 K isotherm, they are negligible for the 573 K isotherm, because in a stagnant lid planet convective stresses become smaller for shallower regions. Here the seismic moment distribution is dominated by the pattern obtained from mantle cooling, that is, regions of thin crust experience a more pronounced cooling compared to regions blanketed by a thick crust (Figures 3g–3i).

4. Discussion

We compare the moment release obtained in this study with previous estimates of Mars' seismicity and with the data obtained for the Moon and the Earth (Figure 4). Previous studies estimated the seismic moment release either from differential cooling of the lithosphere using parametrized thermal evolution models and employing various isotherms (i.e., 573, 873, and 1073 K) to calculate the seismogenic volume (Knapmeyer et al., 2006; Phillips, 1991) or from total slip on surface faults (Golombek, 2002; Golombek et al., 1992). The annual seismic moment release for the Moon has been estimated from shallow moonquakes (Oberst, 1987) and from the recently published deep moonquake data for more than 100 events from three deep moonquake clusters (A01, A06, and A07) (Kawamura et al., 2017). For the Earth, we used the Harvard Centroid Moment Tensor catalog between 1976 and 2013. To compute the moment-frequency distribution for the values obtained in this study, we choose a slope of 0.625, similar to the study of Knapmeyer et al. (2006). This value lies in the interval of [0.6, 0.65], which was obtained from the analysis of quakes on Earth when excluding deep events close to olivine-bridgmanite transition (i.e., 660 km depth on Earth) and events close to mid-ocean ridges (Kagan, 2002). We note that the value of 0.625 seems to fit the size-frequency distribution derived for shallow moonquakes, while the deep moonquake distribution appears to be steeper. However, a larger number of events would be necessary to accurately determine the slope in both cases. In particular, the curvature shown by the shallow moonquake distribution suggests that more small events occurred than were identified in the data recorded by the Apollo network. In addition, rare large events occurring at longer time intervals than the duration of the Apollo seismic experiments may be absent from the catalog. Thus, the catalog might underestimate the lunar seismic moment release.

The moment-frequency relation is sensitive to the largest marsquake assumed and the number of events with a moment larger than or equal to a given seismic moment M_0 increases if the maximum seismic moment is decreased (Figure 4). We adopt a value of 10^{20} Nm that was derived from the analysis of intraplate earthquakes and well-documented normal faults, whose sizes are similar to large normal faults on the border of Valles Marineris (Golombek, 1994). The moment-frequency distribution range calculated from our thermal evolution models is in good agreement with previous estimates and confirms that the seismicity of Mars lies between that of the Moon and the Earth (Figure 4).

In all our simulations we defined the seismogenic lithosphere by using either the 573 K or the 1073 K isotherm. When using the 1073 K isotherm, the stresses produced by mantle convection are similar in magnitude but anticorrelated to the stresses associated with cooling and planetary contraction. This leads to a homogeneous distribution of the annual seismic moment budget. In contrast, for the 573 K isotherm, the contribution from convective stresses is negligible and the distribution of the annual seismic moment budget follows

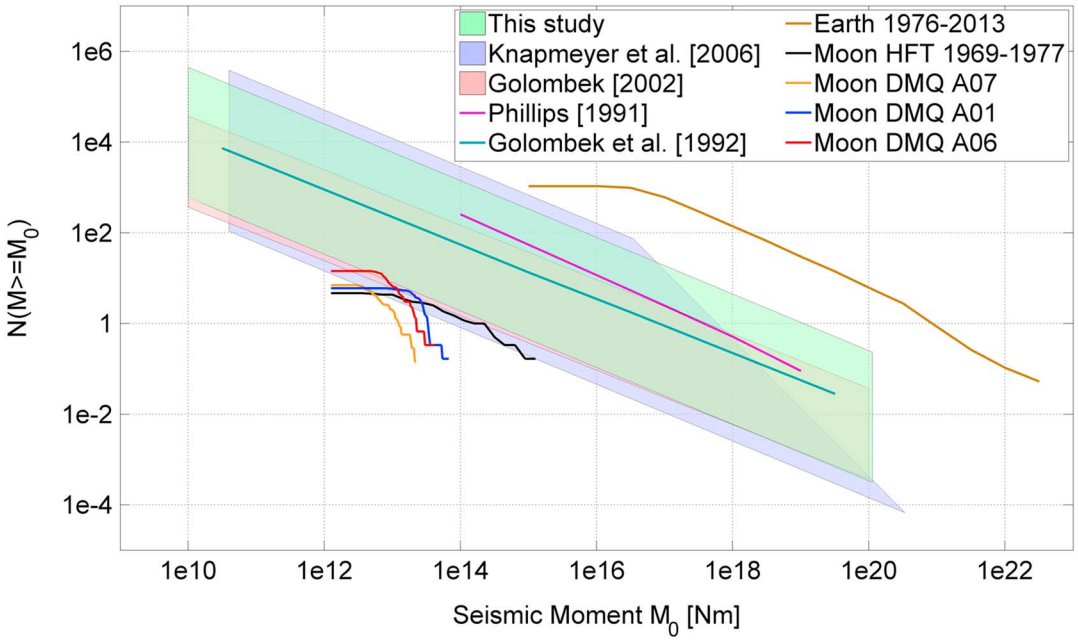

Figure 4. Comparison of moment-frequency relation between previous studies, this work, and the annual seismic moment release of the Earth (Harvard-CMT) and the Moon from both shallow moonquakes and three deep moonquake clusters (A01, A06, and A07). To calculate the moment-frequency-relation, we use the total seismic moment budget, which takes into account the contribution of both stresses from planetary contraction and convective stresses. The value $N(M \geq M_0)$ on the y axis shows the annual number of events with a moment larger than or equal to M_0. The values obtained in this study have been calculated using a slope of 0.625 and a maximum marsquake moment of 10^{20} Nm.

the pattern of the seismic moment based only on planetary cooling, with a larger seismic moment in regions covered by a thin crust. Although the models for which the annual seismic moment budget has been calculated using the 573 K isotherm might seem to contradict the association of faults in and around Tharsis, these faults are most likely due to stresses caused by lithospheric flexure due to loading, which was not considered in this study. However, whether these faults are active today is not known. If indeed these faults are still active, stresses produced by lithospheric flexure would represent an additional contribution to the amount of seismic moment available in the Tharsis region. This contribution will need to be estimated by other studies using flexural models.

The upcoming InSight measurements will help determine the amount and distribution of Martian seismicity by monitoring the seismic activity for one Martian year. Although the mission provides only one seismic station, the presence of depth phases and the relative amplitude of surface waves with respect to body waves will provide constraints on the depth distribution of seismic sources. On Earth, essentially all seismicity below the Moho is connected to plate boundaries and subduction of cold lithosphere. Mars, on the other hand, is a one-plate planet and so far deep seismicity was not expected to exist. This view, however, is challenged by the HC models presented here, which suggest that the seismogenic volume could extend to depths of about 400 km, if the base of the seismogenic layer is marked by the 1073 K isotherm. We note that deep moonquakes, occurring at 800–1,200 km below the lunar surface, represent one of the most numerous types of seismicity on the Moon (Nakamura, 2005). Why the deep moonquakes cluster at this depth is still enigmatic and a number of mechanisms, such as dehydration embrittlement, and transformational faulting have been suggested to explain their occurrence in what should be a ductile regime (Frohlich & Nakamura, 2009). Kawamura et al. (2017) recently proposed that only mantle temperatures of 1240–1275 K are consistent with brittle failure under loading by Earth tidal stresses. Nevertheless, on Mars such deep nucleation zone (800–1,200 km) is unlikely, because the interior temperature rapidly increases to values higher than 1500 K below 600 km depth even for the most depleted mantle. The depth of marsquake foci can be used to distinguish between different seismicity models presented in this study, that is, events originating at depths higher than 180 km would clearly indicate contributions from both cooling and convective stresses while even deeper events (at depths >250 km) would suggest a cold, depleted mantle and a thick crust enriched in HPE. Moreover, the localization

of the seismic events, which can be obtained with the Seismic Experiment for Interior Structure instrument, could also be used to distinguish between an increased seismicity in the northern hemisphere, indicating a shallow seismogenic volume and only a contribution from cooling stresses, and a seismicity distribution that is more homogeneous or slightly larger in the southern hemisphere, suggesting a large seismogenic volume and contributions from both cooling and convective stresses. In addition, the annual seismic moment budget, which will be derived from InSight data, can be used to constrain the seismic efficiency on Mars. If the annual seismic moment budget of Mars lies below 10^{17} Nm, our models indicate a seismic efficiency smaller than 0.05, while a value above 1.95×10^{19} Nm would only be reached if the seismic efficiency is at least 0.5.

5. Conclusion

We have used a series of numerical models of thermal evolution of Mars in a 3-D spherical geometry to assess the magnitude and spatial distribution of present-day Mars' seismicity. We have computed the annual seismic moment budget from 39 thermal evolution simulations for which we have identified three categories of models based on the assumed crustal thickness. We have self-consistently derived the amount and spatial distribution of seismicity from the thermal evolution by taking into account contributions from convective stresses as well as stresses caused by mantle cooling and planetary contraction. Our results predict an annual moment budget between 5.7×10^{16} and 3.9×10^{19} Nm similar to the values presented previously in Phillips (1991); Golombek et al. (1992), Golombek (2002), and Knapmeyer et al. (2006).

The future seismic data to be returned by InSight will better constrain the seismicity of Mars and greatly improve our understanding of the interior of the planet. In particular, the depth of marsquakes and the estimate of the annual seismic moment budget would help distinguish between various models discussed here.

Acknowledgments
All the parameters used in the models and their outcomes are listed in the supporting information. We thank Mark Wieczorek for providing the crustal thickness models used in this study. A.-C. Plesa acknowledges support from the Interuniversity Attraction Poles Programme initiated by the Belgian Science Policy Office through the Planet TOPERS alliance. M. Golombek was supported by the InSight Project, Jet Propulsion Laboratory, California Institute of Technology, under a contract with the National Aeronautics and Space Administration. N. Tosi acknowledges support from the Helmholtz-Gemeinschaft (project VH-NG-1017). Computational time has been provided by the HLRN (project bep00041), which is gratefully acknowledged. This is InSight publication 43. We thank Bruce Banerdt and an anonymous reviewer for their thoughtful comments, which helped to improve a previous version of this manuscript.

References

Anderson, D. L., Duennebier, F. K., Latham, G. V., Toksöz, M. F., Kovach, R. L., Knight, T. C. D., et al. (1976). The Viking seismic experiment. *Science*, *194*(4271), 1318–1321. https://doi.org/10.1126/science.194.4271.1318

Anderson, D. L., Miller, W. F., Latham, G. V., Nakamura, Y., Toksöz, M. N., Dainty, A. M., et al. (1977). Seismology on Mars. *Journal of Geophysical Research*, *82*(28), 4524–4546. https://doi.org/10.1029/JS082i028p04524

Anderson, R. C., Dohm, J. M., Golombek, M. P., Haldemann, A. F. C., Franklin, B. J., Tanaka, K. L., et al. (2001). Primary centers and secondary concentrations of tectonic activity through time in the western hemisphere of Mars. *Journal of Geophysical Research*, *106*(E9), 20,563–20,585. https://doi.org/10.1029/2000JE001278

Anderson, R. C., Dohm, J. M., Haldemann, A. F. C., Hare, T. M., & Baker, V. R. (2004). Tectonic histories between Alba Patera and Syria Planum, Mars. *Icarus*, *171*, 31–38.

Anderson, R. C., Dohm, J. M., Haldemann, A. F. C., Pounders, E., Golombek, M., & Castano, A. (2008). Centers of tectonic activity in the eastern hemisphere of Mars. *Icarus*, *195*(2), 537–546. https://doi.org/10.1016/j.icarus.2007.12.027

Bandfield, J. L., Hamilton, V. E., Christensen, P. R., & McSween, H. Y. (2004). Identification of quartzofeldspathic materials on Mars. *Journal of Geophysical Research*, *109*, E10009. https://doi.org/10.1029/2004JE002290

Banerdt, W. B., Golombek, M. P., & Tanaka, K. L. (1992). Stress and tectonics on Mars. In H. H. Kieffer et al. (Eds.), *Mars* (pp. 249–297). Tucson: University of Ariz Press.

Banerdt, W. B., Smrekar, S., Alkalai, L., Hoffman, T., Warwick, R., Hurst, K., et al. (2012). InSight: An integrated exploration of the interior of Mars. *43rd LPSC, The Woodlands, Texas, Abstract 2838*.

Banerdt, W. B., Smrekar, S., Hoffman, T., Spath, S., Lognonné, P., Spohn, T., et al. (2017). The InSight mission for 2018. *Lunar and Planetary Science XLVIII, The Woodlands, Texas, Abstract 1896*.

Bergman, E. A. (1986). Intraplate earthquakes and the state of stress in oceanic lithosphere. *Tectonophysics*, *132*(1), 1–35. https://doi.org/10.1016/0040-1951(86)90022-3

Carr, M. H. (1974). Tectonism and volcanism of the Tharsis region of Mars. *Journal of Geophysical Research*, *79*(26), 3943–3949.

Dehant, V., Folkner, W., Maistre, S. L., Rosenblatt, P., Yseboodt, M., Asmar, S., et al. (2011). Geodesy on GEMS (GEophysical Monitoring Station). *EPSC-DPS Joint Meeting, Nantes, France, EPSC-DPS2011-1551*.

Frohlich, C., & Nakamura, Y. (2009). The physical mechanisms of deep moonquakes and intermediate-depth earthquakes: How similar and how different? *Physics of the Earth and Planetary Interios*, *173*(3–4), 365–374. https://doi.org/10.1016/j.pepi.2009.02.004

Golombek, M., Kipp, D., Warner, N., Daubar, I. J., Fergason, R., Kirk, R. L., et al. (2017). Selection of the InSight landing site. *Space Science Reviews*, *211*(1), 5–95. https://doi.org/10.1007/s11214-016-0321-9

Golombek, M. P. (1994). Constraints on the largest marsquake. *LPSC XXV, Houston, Texas, Abstract 1221*.

Golombek, M. P. (2002). A revision of Mars seismicity from surface faulting. *LPS XXXIII, Houston, Texas, Abstract 1244*.

Golombek, M. P., Banerdt, W. B., Tanaka, K. L., & Tralli, D. M. (1992). A Prediction of Mars seismicity from surface faulting. *Science*, *258*(5084), 979–981. https://doi.org/10.1126/science.258.5084.979

Golombek, M., & Phillips, R. (2009). Mars tectonics. In T. Watters & R. Schultz (Eds.), *Planetary Tectonics* (Cambridge Planetary Science, pp. 183–232). Cambridge: Cambridge University Press. https://doi.org/10.1017/CBO9780511691645.006

Goossens, S., Sabaka, T. J., Genova, A., Mazarico, E., Nicholas, J. B., & Neumann, G. A. (2017). Evidence for a low bulk crustal density for Mars from gravity and topography. *Geophysical Research Letters*, *44*, 7686–7694. https://doi.org/10.1002/2017GL074172

Grott, M., Breuer, D., & Laneuville, M. (2011). Thermo-chemical evolution and global contraction of Mercury. *Earth and Planetary Science Letters*, *307*, 135–146.

Hahn, B. C., McLennan, S. M., & Klein, E. C. (2011). Martian surface heat production and crustal heat flow from Mars Odyssey gamma-ray spectrometry. *Geophysical Research Letters*, *38*, L14203. https://doi.org/10.1029/2011GL047435

Hauber, E., & Kronberg, P. (2001). Tempe Fossae, Mars: A planetary analogon to a terrestrial continental rift. *Journal of Geophysical Research*, *106*(20), 587–602.
Hauber, E., & Kronberg, P. (2005). The large Thaumasia graben on Mars: Is it a rift. *Journal of Geophysical Research*, *110*, E07003. https://doi.org/10.1029/2005JE002407
Kagan, Y. Y. (2002). Seismic moment distribution revisited: II. Moment conservation principle. *Geophysical Journal International*, *149*, 731–754.
Kawamura, T., Lognonné, P., Nishikawa, Y., & Tanaka, S. (2017). Evaluation of deep moonquake source parameters: Implication for fault characteristics and thermal state. *Journal of Geophysical Research: Planets*, *122*, 1487–1504. https://doi.org/10.1002/2016JE005147
King, S. D., Lee, C., van Keken, P., Leng, W., Zhong, S., Tan, E., et al. (2010). A community benchmark for 2D Cartesian compressible convection in the Earth's mantle. *Geophysical Journal International*, *180*, 73–87. https://doi.org/10.1111/j.1365–246X.2009.04413.x
Knapmeyer, M., Oberst, J., Hauber, E., Wählisch, M., Deuchler, C., & Wagner, R. (2006). Working models for spatial distribution and level of Mars' seismicity. *Journal of Geophysical Research*, *111*, E11006. https://doi.org/10.1029/2006JE002708
Lognonné, P., Banerdt, W. B., Weber, R. C., Giardini, D., Pike, W. T., Christensen, U., et al. (2015). Science goals of SEIS, the InSight seismometer package. 46th Lunar and Planetary Science Conference, LPI Contribution No. 1832. (pp. 2272). Woodlands, TX. 16–20 March.
Lorenz, R. D., Nakamura, Y., & Murphy, J. R. (2017). Viking-2 seismometer measurements on Mars: PDS data archive and meteorological applications. *Earth and Space Science*, *4*, 681–688. https://doi.org/10.1002/2017EA000306
Nakamura, Y. (2005). Farside deep moonquakes and deep interior of the Moon. *Journal of Geophysical Research*, *110*, E01001. https://doi.org/10.1029/2004JE002332
Neumann, G. A., Zuber, M. T., Wieczorek, M. A., McGovern, P. J., Lemoine, F. G., & Smith, D. E. (2004). Crustal structure of Mars from gravity and topography. *Journal of Geophysical Research*, *109*, E08002. https://doi.org/10.1029/2004JE002262
Oberst, J. (1987). Unusually high stress drops associated with shallow moonquakes. *Journal of Geophysical Research*, *92*, 1397–1405.
Phillips, R. J. (1991). Expected rates of marsquakes, in scientific rationale and requirements for a global seismic network on Mars (LPI Tech. Rep., 91-02 LPI/TR-91-02, 35–38). Houston, Texas: Lunar and Planet Inst.
Plesa, A.-C., Grott, M., Tosi, N., Breuer, D., Spohn, T., & Wieczorek, M. A. (2016). How large are present-day heat flux variations across the surface of Mars? *Journal of Geophysical Research: Planets*, *121*, 2386–2403. https://doi.org/10.1002/2016JE005126
Sautter, V., Toplis, M. J., Beck, P., Mangold, N., Wiens, R., Pinet, P., et al. (2016). Magmatic complexity on early Mars as seen through a combination of orbital, in-situ and meteorite data. *Lithos*, *254*, 36–52. https://doi.org/10.1016/j.lithos.2016.02.023
Scholz, C. H. (1998). Earthquakes and friction laws. *Nature*, *391*, 37–42.
Spohn, T., Grott, M., Smrekar, S., Krause, C., Hudson, T., & HP^3 Instrument Team (2014). Measuring the Martian heat flow using the heat flow and physical properties package (HP^3). *45th Lunar and Planetary Science Conference, The Woodlands, Texas, Abstract 2838*.
Tanaka, K. L. (1990). Tectonic history of the Alba Patera-Ceraunius Fossae region of Mars. In *20th LPSC* (pp. 515–523). Houston, Texas.
Tanaka, K. L., & Davis, P. A. (1988). Tectonic history of the Syria Planum province of Mars. *Journal of Geophysical Research*, *93*(14), 893–917.
Tanaka, K. L., Golombek, M. P., & Banerdt, W. B. (1991). Reconciliation of stress and structural histories of the Tharsis region of Mars. *Journal of Geophysical Research*, *93*(15), 617–633.
Taylor, G. J., Boynton, W., Brückner, J., Wänke, H., Dreibus, G., Kerry, K., et al. (2006). Bulk composition and early differentiation of Mars. *Journal of Geophysical Research*, *111*, E03S10. https://doi.org/10.1029/2005JE002645
Taylor, J., Teanby, N. A., & Wookey, J. (2013). Estimates of seismic activity in the Cerberus Fossae region of Mars. *Journal of Geophysical Research: Planets*, *118*, 2570–2581. https://doi.org/10.1002/2013JE004469
Tosi, N., Grott, M., Plesa, A.-C., & Breuer, D. (2013). Thermochemical evolution of Mercury's interior. *Journal of Geophysical Research: Planets*, *118*, 2474–2487. https://doi.org/10.1002/jgre.20168
Ward, S. N. (1998a). On the consistency of earthquake moment rates, geological fault data, and space geodetic strain: The United States. *Geophysical Journal International*, *134*, 172–186.
Ward, S. N. (1998b). On the consistency of earthquake moment rates, geological fault data, and space geodetic strain: Europe. *Geophysical Journal International*, *135*, 1011–1018.
Wänke, H., & Dreibus, G. (1994). Chemistry and accretion of Mars. *Philosophical Transactions of the Royal Society London*, *A349*, 2134–2137.
Wiens, D. A., & Stein, S. (1983). Age dependence of oceanic intraplate seismicity and implications for lithospheric evolution. *Journal of Geophysical Research*, *88*(B8), 6455–6468. https://doi.org/10.1029/JB088iB08p06455
Wise, D. U., Golombek, M. P., & McGill, G. E. (1979). Tectonic evolution of Mars. *Journal of Geophysical Research*, *84*, 7934–7939.
Zuber, M. T. (2001). The crust and mantle of Mars. *Nature*, *412*, 220–227.